Image Cover Sheet

CLASSIFICATION	SYSTEM NUMBER 507220
UNCLASSIFIED	

TITLE

MICROSTRUCTURAL CHARACTERIZATION OF LASER-CLAD NICKEL ALUMINUM BRONZE ALLOYS BY TEM

System Number:

Patron Number:

Requester:

Notes: Paper #17 contained in Parent Sysnum #507203

Microstructural Characterization of Laser-Clad Nickel Aluminum Bronze Alloys by TEM

by

J.C. Bennett, Department of Physics, Acadia University

and

C.V. Hyatt, Defence Research Establishment Atlantic

ABSTRACT

Recently, the use of high power lasers for surface melting and cladding of nickel aluminum bronze (NAB) components has stimulated renewed interest in the microstructural development of these alloys. In this study, a laser-clad NAB weldment of nominal composition Cu - 9 wt. % Al - 5 wt. % Ni - 4 wt. % Fe - 1 wt. % Mn, provided by DREA was examined using transmission electron microscopy. Significant variations in the microstructure were observed between the weld deposit and heat affected zone of the clad. In the weld deposit, the microstructure predominantly consisted of two phases which are the product of martensitic or possibly bainitic phase transformations. A high density of Fe-rich precipitates, ranging up to 200 nm in size, are also distributed throughout both matrix phases. In the heat affected zone, the microstructure typically contained three major phases: a martensitic phase similar to that observed in the deposit region, the fcc α phase, and an ($\alpha + \kappa$) eutectoid. The small Fe-rich precipitates are retained in the martensitic phase. The observed phase relationship and morphologies will be discussed in terms of the transformation behaviour of the NAB clad.

Microstructural Characterization of Laser-Clad Nickel Aluminum Bronze Alloys using Transmission Electron Microscopy

INTRODUCTION

Nickel aluminum bronze (NAB) alloys are used for many marine applications due to their excellent sea water corrosion resistance and good mechanical properties. At the Defence Research Establishment Atlantic, laser surface modification techniques such as cladding and surface melting are being investigated for the repair and surface engineering of NAB alloy components [1]. In these processes, a high intensity laser is focussed to melt a thin surface layer [2]. Since the melting occurs over a very short time, the bulk of the component remains cool and acts as an infinite heat sink. The consequent very rapid self-quenching and resolidification which occurs may in turn generate metastable phases. Currently, there is little data available concerning the microstructures produced in laser processed NAB alloys. In this paper, transmission electron microscopic (TEM) observations of the microstructure developed in a commercial (C95800) NAB alloy cladding are reported.

NAB alloys of interest for marine applications typically contain from 8 to 13 wt.% Al, 4 to 5 wt.% Ni, and 4 to 5 wt.% Fe along with smaller amounts of Mn and Si. To facilitate discussion of the microstructural features found in these alloys, the relevant vertical section of the equilibrium phase diagram is shown in Figure 1 [3]. For NAB alloys with Al contents near 10 wt.%, the solid solution β phase with bcc crystal structure is stable at high temperatures. Upon cooling, proeutectoid α with fcc crystal structure precipitates along with several ordered intermetallic phases, collectively referred to as κ. In quenched samples, a metastable β' phase may also be observed with a volume fraction dependent on the degree of undercooling. Several previous studies [4,5] have indicated that the β' phase is the product of a martensitic phase transformation. The crystallographic data reported for the various phases in the NAB phase diagram are summarized in Table 1.

Several previous investigations of the microstructure of NAB alloys in the as-cast and tempered condition have been carried out using TEM [6-8]. However, for laser clad and laser surface melted NAB alloys, only limited microstructural data is currently available [5,8,9]. These studies indicate that laser processed NAB alloys contain novel

precipitate and matrix phases whose stability is sensitively determined by alloy composition and cooling rate from the β field. It is thus important to characterize laser processed materials under conditions corresponding as closely as possible with actual metallurgical practice.

EXPERIMENTAL

The NAB weldment studied was supplied by DREA and produced using a laser cladding technique described previously [1]. Briefly, a coupon of composition Cu - 8.6 wt.% Al - 4.8 wt.% Ni - 4.0 wt.% Fe - 1.1 wt.% Mn was clad by scanning a laser beam while simultaneously feeding a welding wire of composition Cu - 9.0 wt.% Al - 4.6 wt.% Ni - 3.9 wt.% Fe - 1.2 wt.% Mn into the melt pool. The resultant deposit was composed of small overlapping beads which were directly related in size to the dimensions of the melt pool during the single scan of the beam. A laser beam heat input of 1.2 kJ/cm was used for these experiments. Figure 2 shows schematically a section of the clad deposit with the location of the as-deposited, reheat and heat affected zones indicated.

Specimens for TEM were obtained by sectioning the coupon parallel to the clad surface using a low speed saw. A surface layer from 0.1- 0.3 mm thick was removed and then the sections were backed thinned to 0.1 mm using a range of SiC grinding papers (240-600 grit). After punching the 3 mm diameter disks required for TEM, further mechanical polishing reduced the thickness to ~100 μm. Since the deposit region is known to extend to a depth of at least 1000 μm under these laser processing conditions, the above procedure limited examination to the as-deposited and reheat zones of the cladding.

The 3 mm disks were thinned to electron transparency in a Tenupol-3 jet electropolisher using a 33 % nitric acid/methanol solution. It was observed that attainment of the polishing condition depended very sensitively on the experimental parameters. For example, cooling of the electrolyte in the range -30 to -40 °C was essential to avoid extensive pitting of the specimens. The optimum polishing condition was obtained with a potential difference of 11 V and a slow to moderate electrolyte flow speed which resulted in a polishing current of 0.2 - 0.25 A. Larger currents invariably resulted in etching rather than polishing of the specimens.

The position of the electron transparent region with respect to the as-deposited and

reheat zones was established by visual inspection using a stereomicroscope. The procedure consisted of replacing the polished 3 mm disks within the sections which had been previously etched in $FeCl_3$/HCl/methanol solution to reveal the zones of interest. In addition, the sections were also mounted for optical microscopy in plan view.

Electron microscopy of the thin foils was carried out with either PHILIPS EM300 or CM20 transmission electron microscopes operating at 100 and 200 kV, respectively. Microanalysis of selected phases in the thin foil specimens was performed with the CM20 microscope using an energy-dispersive x-ray detector. Quantitative analysis was obtained using the ratio technique [11] and calculated k-factors.

RESULTS

Typical optical micrographs obtained for the as-deposited and reheat zones are shown in Figure 3. The observed microstructures are similar to those reported previously for laser clad NAB alloys [1,2,12]. Light etching material is generally observed on the prior β grain boundaries and as elongated rods within the grains, corresponding to allotriomorphic and Widmanstatten α, respectively. The dark etching regions have usually been interpreted as martensite. For the claddings, comparable microstructures were observed in the as-deposited and reheat zones, however the Widmanstatten α plates were considerably coarsened in the latter case. The results of the optical metallography confirmed that all of the specimens examined in the TEM were representative of either the as-deposited or reheat zones of the cladding.

Figure 4 shows a typical TEM micrograph of the as-deposited region and reveals a predominantly dual phase microstructure consisting of lighter contrast (more electron transparent) rods separated by irregular, darker contrast plates. A pronounced acicular morphology for the rods was evident within the former β grain interiors. In addition, a high density of small (~20 nm), roughly cuboidal precipitate particles were dispersed throughout both the rods and plates. X-ray microanalysis of the rods and plates yielded similar results, close to the nominal composition of the bulk coupon, with only small differences in Al and Ni content between the two regions. Conversely, the precipitates were substantially enriched in Fe and Ni in comparison to the bulk (Table 2).

Selected area electron diffraction (SAD) and diffraction contrast imaging of the acicular rods suggests several variants may be present in the as-deposited region. A relatively small fraction of the rods were distinguished by varying numbers of stacking faults appearing in isolation or in clusters (Figure 5). Analysis of the SAD patterns revealed a crystal structure based on the fcc unit cell with a lattice parameter of ~0.375 nm, confirming that these rods are composed of Widmanstatten α. Convergent beam electron diffraction (CBED) patterns obtained using a probe ~15 nm diameter (Figure 6) are consistent with the space group Fm3m expected for the fcc α phase. The CBED analysis also revealed no orientational change occurred on crossing the positions of the faults, confirming their displacive nature. No evidence of solute ordering was detected in the SAD or CBED patterns.

The majority of the rods in the as-deposited region contained a uniform density of stacking faults spaced about 0.6 nm apart (Figure 7). Superimposed on this regular array of defects, random faulting was also observed. The SAD patterns from the rods revealed pronounced streaking of the diffraction spots, associated with the random faulting, as well as additional satellite reflections. As a result, the observed SAD patterns could not be indexed as any simple close-packed crystal structure such as fcc or hcp (hexagonal close-packed). The presence of the stacking fault array indicated that the most suitable crystallographic description for this phase was in terms of an interface modulation of the fcc structure of the parent α phase via the periodic insertion of stacking faults on every third close-packed plane. Similar interface modulated superstructures have been reported for martensitic phases arising in some NAB and related alloys [9,13,14].

The interface modulated superstructure described above is generated through the periodic repetition of modules consisting of close-packed layers separated by stacking faults on the $\{111\}_{fcc}$ planes. For such an interface modulation, satellite reflections occur at positions shifted relative to those of the parent structure by an amount inversely related to the period of the faulting [15]. Rather than using an fcc unit cell, it is convenient to specify the satellite shifts based on a primitive hexagonal unit cell with the c-axis chosen perpendicular to the close-packed plane. Using this approach, the position of the parent (1100) reflection is located geometrically and taken as a reference point for measurements

of the fractional shifts. In the observed SAD patterns, the k = 1 and k = -1 satellites were shifted in opposite directions, indicating a rhombohedral symmetry for the modulation. Information on the stacking mode can also be deduced from the intensity distribution of the satellites. SAD patterns calculated on the basis of a 9 layer stacking module (ABCBCACAB where A, B and C are close-packed planes) were found to be in good agreement with the experimental intensities (Figure 8). The SAD patterns can thus be indexed as an unordered 9R structure.

TEM observations of the irregular, dark plates revealed that these were composed of narrow, acicular lamellae ranging in width from 10-50 nm (Figure 9a). Stacking faults spaced ~0.6 nm apart may also be observed within the twin lamellae in high magnification images (Figure 10). While the streaking of the diffraction spot renders SAD patterns difficult to measure accurately, the results were generally consistent with an interface modulated 9R superstructure. In addition, SAD showed that the lamellae were twin-related with twinning occurring on the {200}fcc planes (Figure 9b). Elongation of the diffraction spots along the direction of twinning suggests the interface is not fully coherent. Similar finely twinned martensites have been previously observed in quenched NAB alloys [4].

The martensite lamellae and the 9R α phase rods were crystallographically identical, however the difference in scale suggests these features formed under differing thermal regimes. In addition, EDX microanalysis indicated that the martensite was enriched in Al relative to the 9R α phase. Note also that the observed similarity in electron transparency, morphology and chemical composition indicates a close relationship exists between the fcc and 9R α phases. Hence, the TEM observations would appear to be consistent with a bainitic origin for the 9R α phase. However, due to the presence of several precipitation reactions which complicate the interpretation of the compositional data, further studies are needed to definitively establish the nature of the 9R α phase.

A high density of small, cuboidal precipitates were characteristically observed in both the martensite and 9R α phases. The precipitates ranged from 20-50 nm in size and were Fe-rich according to EDX microanalysis. A typical distribution of precipitates in the 9R α phase (orientated with the stacking faults out of contrast) is shown in Figure 11. For

precipitates very near the edge of the foil, it was occasionally possible to obtain electron microdiffraction (MD) patterns, which were free of intensity contributions from the surrounding matrix. (Figure 11 inset). The MD patterns were indexed in terms of an ordered B2 crystal structure, suggesting that these precipitates are related to the κ_{IV} or κ_{II} particles previously reported to occur in cast NAB alloys. The precipitates in the martensite exhibited a similar size distribution, chemical composition, morphology and crystal structure as those in the 9R α phase.

It was not possible to deduce a consistent orientational relationship between the precipitate and matrix phases based on the MD studies. However, it was very difficult in practice to locate high symmetry zone axes for all but the largest of the precipitate particles, i.e. those approaching 50 nm in size. In the TEM images, characteristic "lobe" diffraction contrast associated with coherency strain fields was often observed around the smaller precipitates. This suggests that there exists a critical precipitate size for loss of coherency in this system. Such a critical size effect would normally occur if the surface energy of the precipitates becomes small relative to the coherency strain energy as the particle size increases. A coherency size effect of this type may account for the observation of ring diffraction patterns formed by the precipitates in SAD patterns obtained using a large area-selecting aperture (Figure 12). The intensity in these ring patterns would be expected to be dominated by contributions from the largest precipitate particles, which are incoherent with the matrix phases. Further studies are in progress to ascertain the influence of precipitates on mechanical properties and grain refinement in NAB alloys.

The microstructure observed in the reheat zone of the cladding is broadly similar to that described above for the as-deposited region. However, in the reheat zone, the α phase contained very few precipitates, was largely free from stacking faults and in many areas adopted an equiaxed rather than rod-like morphology. SAD and CBED analyses indicated an fcc crystal structure with space group $Fm\bar{3}m$ for the α phase in the reheat zones. No α particles having the 9R crystal structure were detected. The martensite in the reheat zones is crystallographically identical to that in the as-deposited regions, retaining the 9R structure and a high density of Fe-rich precipitates. While the average plate size was

somewhat reduced, the martensite still consisted of narrow, twin-related lamellae ranging from 10-50 nm in width. The size, morphology and crystal structure of the precipitates found in the martensite was also unchanged.

In many parts of the reheat zone, a microstructure consisting of a light contrast phase containing numerous elongated precipitate particles was observed (Figure 13). SAD, CBED and EDX microanalysis indicated that the matrix corresponded to the fcc α phase described above while the elongated precipitates were considerably different from those observed elsewhere. SAD patterns from the precipitates were indexed in terms of a B2 structure with lattice parameter a = 0.26 nm. EDX microanalysis yielded an average composition of 24 wt.% Cu - 27 wt.% Al - 29 wt.% Ni - 20 wt.% Fe, indicating that the elongated precipitates were Ni-rich in contrast to the cuboidal, Fe-rich precipitates found in the martensite, 9R α and fcc α phases. The morphology, unit cell and composition of the elongated precipitates is similar to that reported by Hasan et al. for κ_{III} particles in as-cast NAB alloys [6]. The TEM observations are consistent with the formation of ($\alpha + \kappa_{III}$) eutectoid in the reheat zone. Within these eutectoid areas, the α phase was predominantly present as grain boundary allotriomorphs rather than Widmanstatten plates. Note that limited eutectoid formation also occurred in the vicinity of prior β grain boundaries within the as-deposited regions of the cladding.

DISCUSSION

The phases observed in the present TEM study are consistent with the results of previous studies of laser-processed NAB alloys. The most extensive work has been performed by Liu and co-workers [5,9,16] who examined a NAB laser-cladding produced on an aluminum substrate. These workers identified two types of martensite which were designated sheet or lath based on their morphology. The sheet martensite had a 9R structure and corresponds to the martensitic phase identified in the present study while the lath martensite, which had a fcc crystal structure, would appear to correspond to either the 9R or pro-eutectoid α phase reported here.

The formation of Fe-rich precipitates in NAB alloys has been reported by several workers [6,8,16]. Most of these studies have concluded that the Fe-rich precipitates form

prior to the martensitic transformation. In the current study, the observation in SAD patterns of "spotty" diffraction rings produced by the precipitates, suggesting some degree of preferred orientation, supports this conclusion. Hence, the TEM results indicate that the decomposition of β to $\alpha + \kappa_{IV}$ occurs well above the martensite start temperature, M_s.

No direct evidence regarding the role of solute diffusion in the transformation producing the α phase is currently available. However, the results of Hasan et al. [6] for cast NAB alloys indicate that Widmanstatten α precipitates from the β phase under conditions where diffusion is likely to be important. From a crystallographic point of view, the 9R α phase and martensite have similar interface modulated superstructures with a high density of randomly occurring stacking faults. EDX analysis indicates that the Al content of the 9R α phase is slightly lowered while the plate size is much larger relative to that of the twin-related lamellae in the martensite, implying these features formed under different temperature conditions. The TEM observations are therefore consistent with a bainitic origin for Widmanstatten α having the 9R structure. Similar bainitic phases have been reported in the Cu-Al-Ni [14] and Cu-Al-Zn [17] alloy systems.

Due to the steepness of solubility lines, the mechanisms governing the phase stability in both the as-deposited and reheat zones of the cladiing depend sensitively on composition as well as cooling rate. Although further studies are required to obtain a detailed understanding of these processes, the TEM results point to the following general model. NAB initially solidifies as the bcc β phase and, upon further cooling, decomposes to the α phase precipitates from β, probably via a bainitic transformation. The presence of Ni and/or Fe alloying elements apparently lowers the temperature for the β to $\alpha + \kappa_{III}$ eutectoid reaction below that required for the formation of the Fe-rich, κ_{IV} type precipitates. Nucleation of the Al depleted 9R bainitic α phase, perhaps aided by the presence of stress gradients around the κ_{IV} precipitates, produces a supersaturation of Al in the remaining parent β phase, depressing M_s. [3]. As a result, the martensitic transformation probably occurs at a relatively low temperature. The observation of substantial amounts of martensite in the as-deposited region indicates that a high cooling rate prevails during laser cladding. This rapid cooling gives the α plates little opportunity

to coarsen and produces a fine Widmanstatten morphology in the as-deposited region of the cladding.

A short heating pulse from the scanning laser beam, which is again followed by fairly rapid cooling, is responsible for the microstructural changes occurring in the reheat zone. The reheat temperature profile produced during cladding has not yet been established. However, the similarity of the martensite in the as-deposited and reheat zones indicates that the martensite retransformation temperature is increased above the peak reheat temperature, possibly due to stabilization by the Fe-enriched particles. This is consistent with the results of Liu et al. [5] who observed no noticeable change in the sheet martensite on heating between room temperature and 673 K. It would appear that the maximum reheat temperature is sufficient to dissolve the κ_{IV} type precipitates in the α phase. . Although further studies of the tempering behaviour of ternary NAB alloys are required, it seems likely that the bainite transforms to the stable fcc α phase through a gradual reduction in the stacking fault density. Elimination of the bainite proceeds via a diffusion-controlled disordering mechanism and could occur at relatively low reheat temperatures. The TEM observations suggest this process also occurs in the as-deposited region but is often only partially completed.

The results of the present study demonstrate that TEM can provide considerable new insights into the complex microstructural phenomena occurring in laser processed NAB alloys. It is evident that diffusionless and diffusional transformations, precipitation reactions, twinning and long-range ordering all play important roles in forming the microstructures.

REFERENCES

1. C.V. Hyatt, K.H. Magee, J. Hewitt and T. Betancourt, Proc. Of 2nd CF/CRAD Meeting on Naval Applications of Materials Technology, J.R. Matthews, ed., Halifax, 1995.
2. C.V. Hyatt and K.H. Magee, Proc. Of Advanced Methods of Joining New Materials II, The Am. Weld. Soc., Miami, 1994, 111-126.
3. P. Bezina, Int. Metals Rev., **27**, 1982, 77-121.
4. F. Hasan, G.W. Lorimer and N. Ridley, J. de Physique, C4, supp. 12, **43**, 1982, 651-657.
5. Y. Liu, J. Mazumder and K. Shibata, Metall. And Mat. Trans. A, **25A**, 1994, 37-46.
6. F. Hasan, A. Jahanafrooz, G.W. Lorimer, and N. Ridley, Metall. Trans., **13A**, 1982, 1337-1345.
7. F. Hasan, G.W. Lorimer and N. Ridley, Metals Sci., **17**, 1983, 289-295.
8. D.E. Bell, M.Sc. Thesis, Penn. State Univ., 1993.
9. Y. Liu, J. Mazumder and K. Shibata, Acta metall. mater, **42**, 1994, 1755-1762.
10. J. Hewitt and V.E. Merchant, Proc. Of 2nd CF/CRAD Meeting on Naval Applications of Materials Technology, J.R. Matthews, ed., Halifax, 1995.
11. G. Cliff and G.W. Lorimer, J. Microscopy, **103**, 1975, 1397-1399.
12. J.A. Gianetto, M. Sahoo, M.W. Letts and C. Bibby, DREA report CR/95/435, Defence Research Establishment Atlantic, 1995.
13. P. Ratchev, J. Van Humbeeck and L. Delaey, Acta metall. mater., 41, 1993,2441-2449.
14. Y.S. Sun, G.W. Lorimer and N. Ridley, Metall. Trans.,21A, 1990, 575- 588.
15. S. Amelinckx and D. Van Dyck, Electron Diffraction Techniques, J.M. Cowley, ed., Oxford Univ. Press, 1995.
16. Y. Liu, M.E. Mochel, J. Mazumder and K. Shibata, Acta metall. mater., **42**, 1994, 1763-1768.
17. K. Takezawa and S. Sato, Metall. Trans., **21A**, 1990, 1541-1545.

Phase	Structure Prototype	Schnoeflies Designation	Space Group	Lattice Spacing (nm)
α	Cu	A1	Fm3m	0.365
β'	Cu₃Al	9R	R3̄m	—
κ$_{II}$,κ$_{IV}$	Fe₃Al	B2	Fm3m	0.571
κ$_{III}$	NiAl	B2	Pm3m	0.288

Table 1: Crystallographic data for the various phases observed in as-cast NAB alloys [6].

Description	Cu	Al	Ni	Fe	Mn
fcc α phase (reheat zone)	0.846 ±.019	0.070 ±.014	0.046 ±.012	0.031 ±.004	0.007 ±.001
9R α phase (deposit)	0.865 ±.014	0.076 ±.003	0.041 ±.007	0.013 ±.003	0.005 ±.002
martensite	0.821 ±.030	0.097 ±.011	0.053 ±.014	0.016 ±.006	0.008 ±.001
κ$_{III}$ precipitates	0.243 ±.015	0.268 ±.014	0.292 ±.024	0.197 ±.010	
κ$_{IV}$ precipitates	0.449 ±..117	0.105 ±.014	0.119 ±.044	0.268 ±.135	0.006 ±.003

Table 2: Results of chemical analysis (wt. %) by EDX of Phases in NAB Laser Cladding.
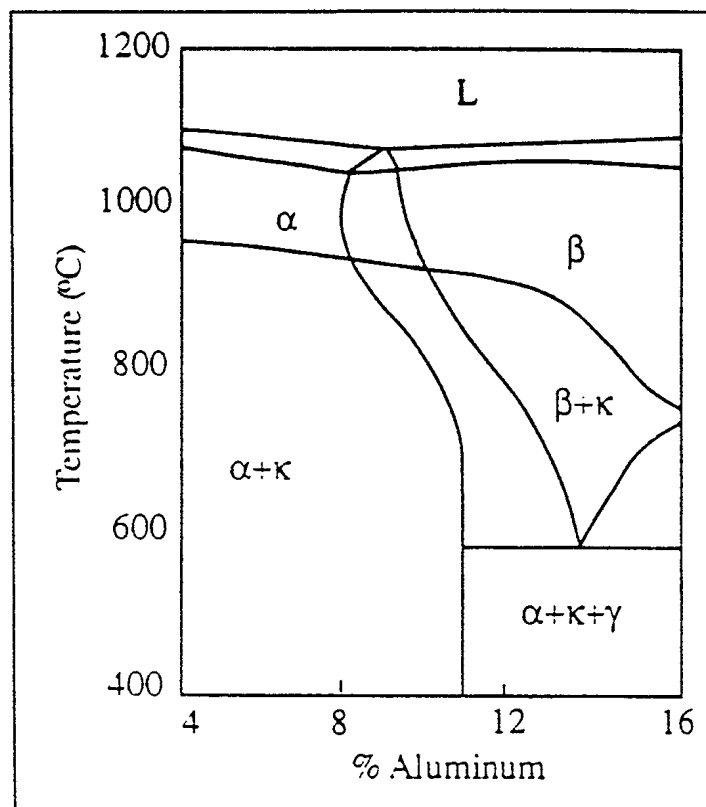
Figure 1: Vertical section of the Cu-Al-5 wt. % Ni-5 wt. % Fe equilibrium phase diagram [3].
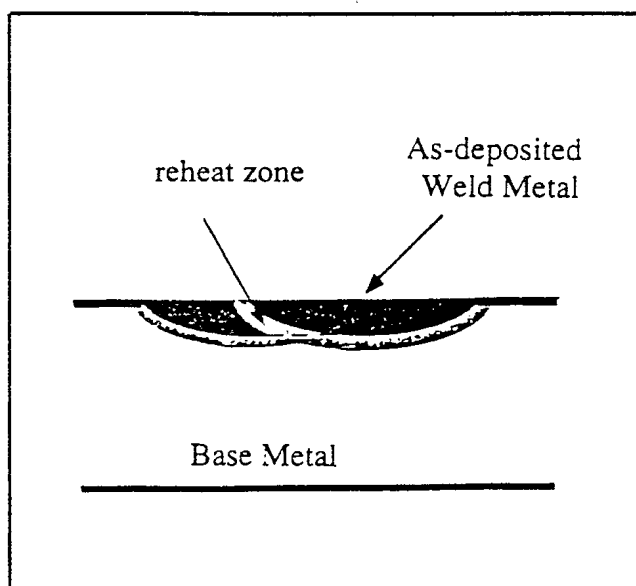
Figure 2: Schematic diagram of the various zones of the laser-clad weldment.
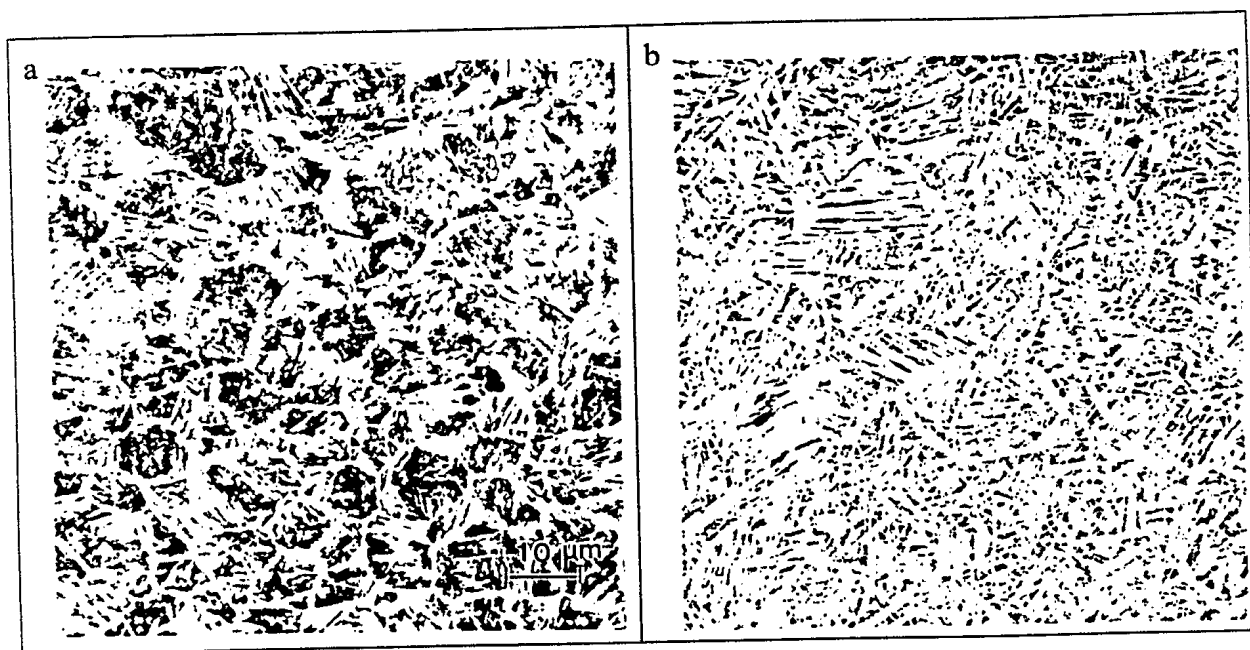

Microstructural Characterization of Laser Clad NAB Alloys using TEM

Figure 3: Optical micrographs showing typical microstructures for (a) the as-deposited and (b) reheat zones of a NAB laser cladding.
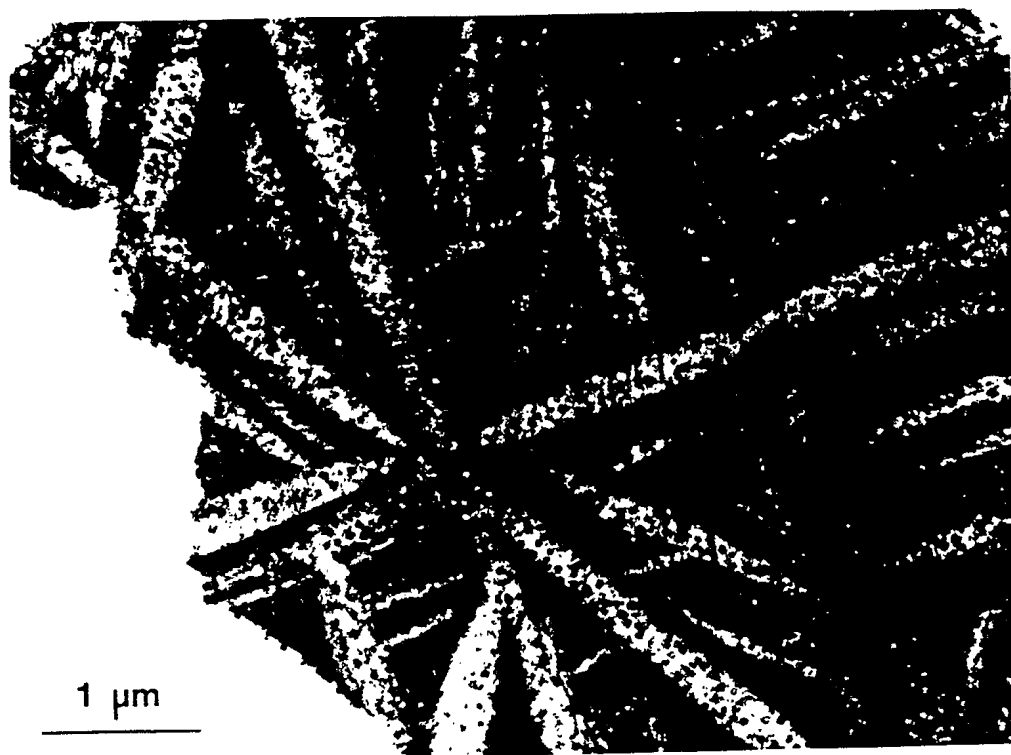

1 μm

Figure 4: Typical TEM micrograph of the as-deposited region-of a NAB laser cladding showing Widmanstatten α rods (light) and martensite plates (dark).

Figure 5: TEM image of a fcc α rod in the as-deposited region showing clusters of stacking faults. Moire ringes, arising from double diffraction, are frequently observed.

Figure 7: TEM image of an α rod with 9R long-range order. Closely spaced, parallel striations visible in the image are a periodic array of stacking faults on the $\{111\}_{fcc}$ planes..
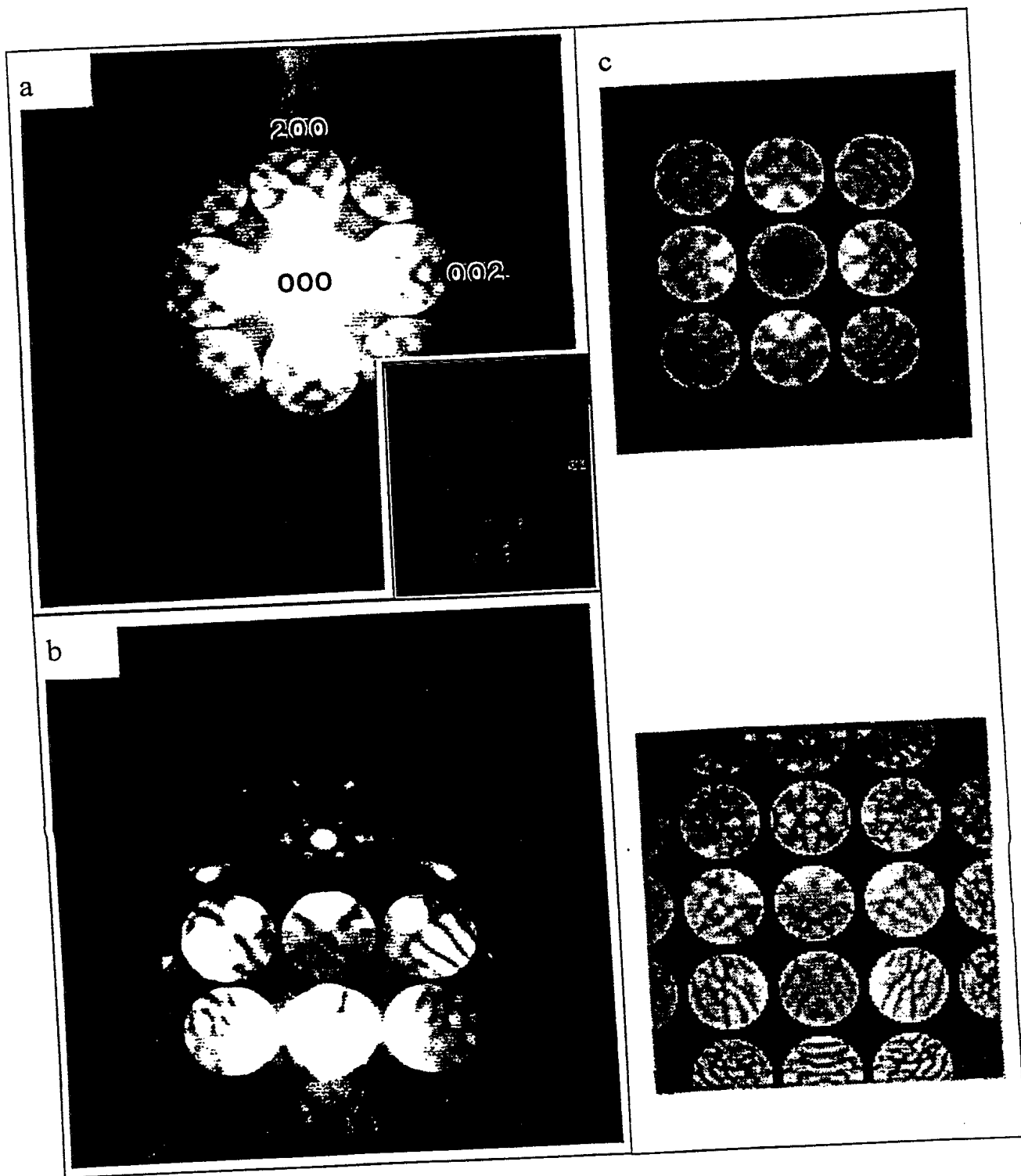
Figure 6: [100] zone axis CBED patterns for the Widmanstatten α phase. (a) On-axis pattern showing 4mm symmetry (the central disk is shown in the insert). (b) Dark-field pattern tilted such that the center of the Laue circle is at the position of the (200) disk. (c) Simulated CBED patterns for space group $Fm\bar{3}m$.
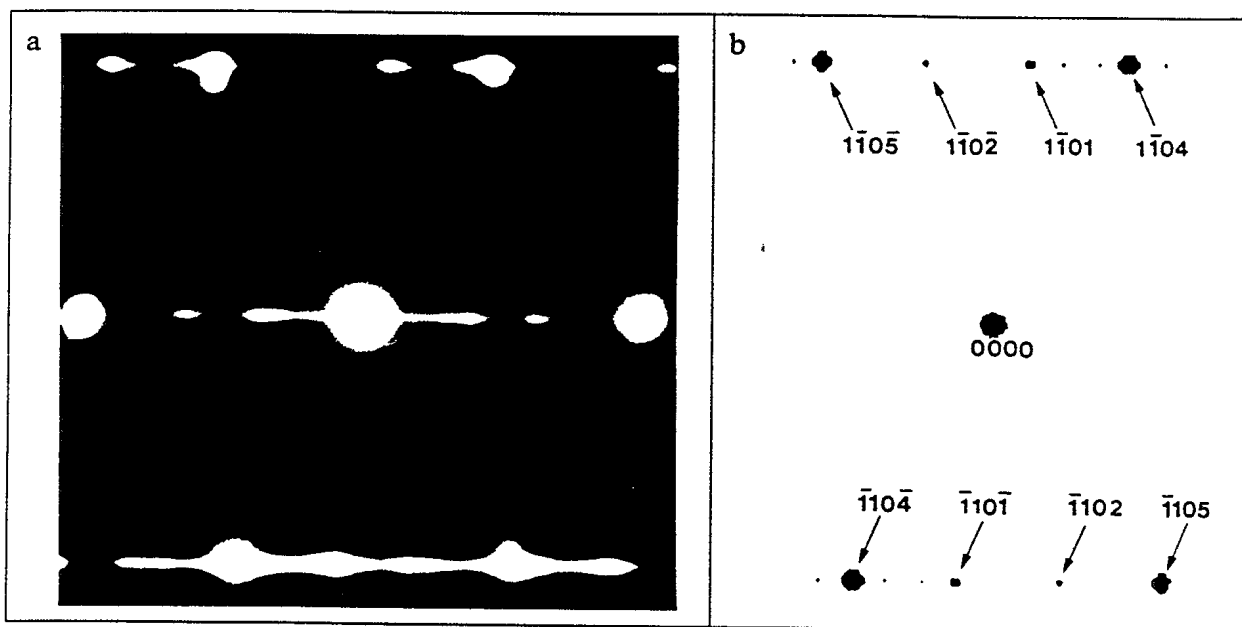
Figure 8: (a) [11$\bar{2}$0] zone axis SAD pattern for the long-range ordered 9R α phase. (b) Corresponding calculated pattern for a ABCBCACAB stacking module.
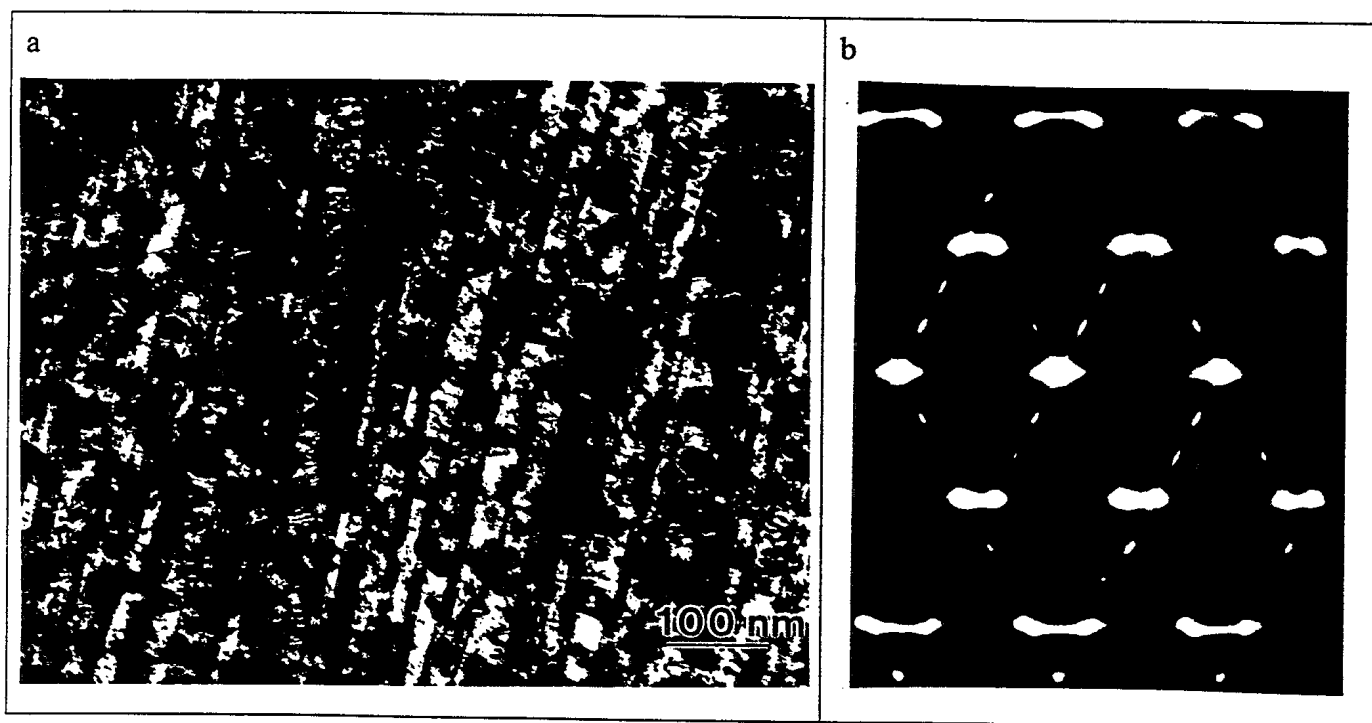

Figure 9: (a) TEM micrograph of martensite in the as-deposited region showing parallel-sided, acicular twins. (b) Corresponding [11$\bar{2}$0] zone axis SAD pattern for the martensite revealing the presence of 9R order and twinning

Figure 10: TEM image of the martensite lamellae showing the scale of the twin domains and numerous stacking faults.
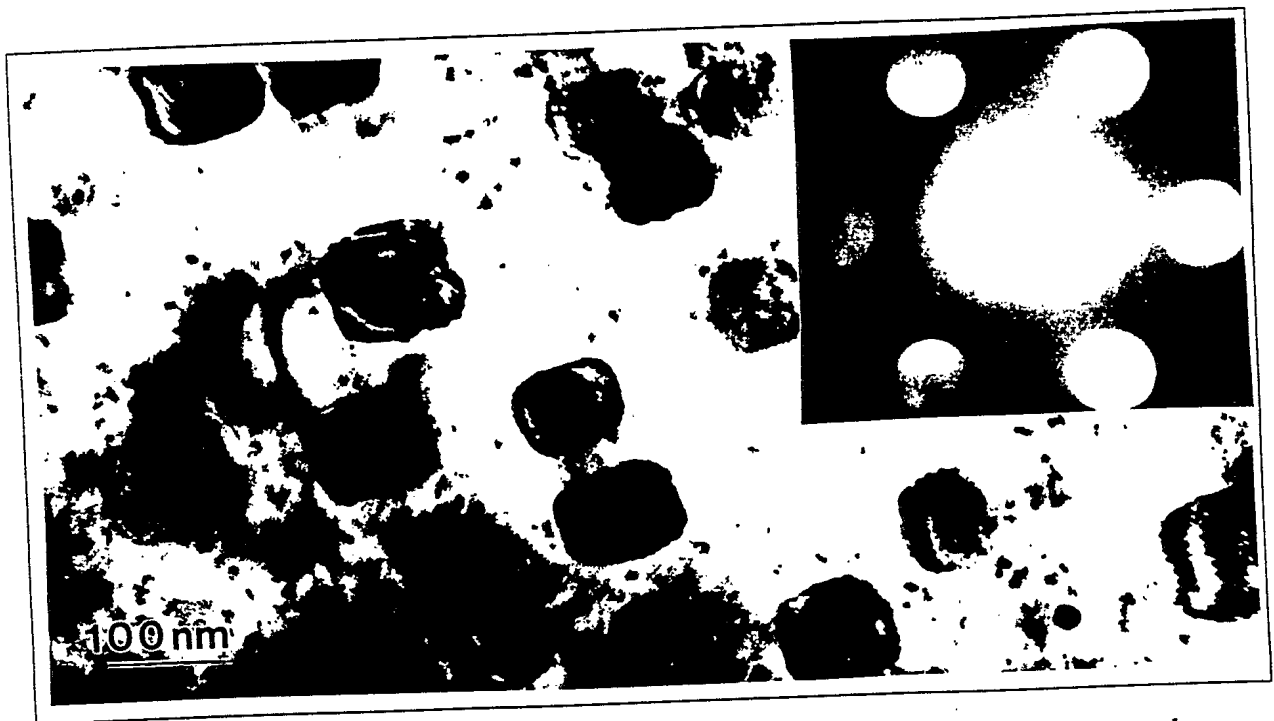

Figure 11: TEM image showing cuboidal, Fe-rich precipitates within the 9R α phase. Microdiffraction patterns (inset, [111] zone axis) indicate the precipitates possess B2 crystal structure.
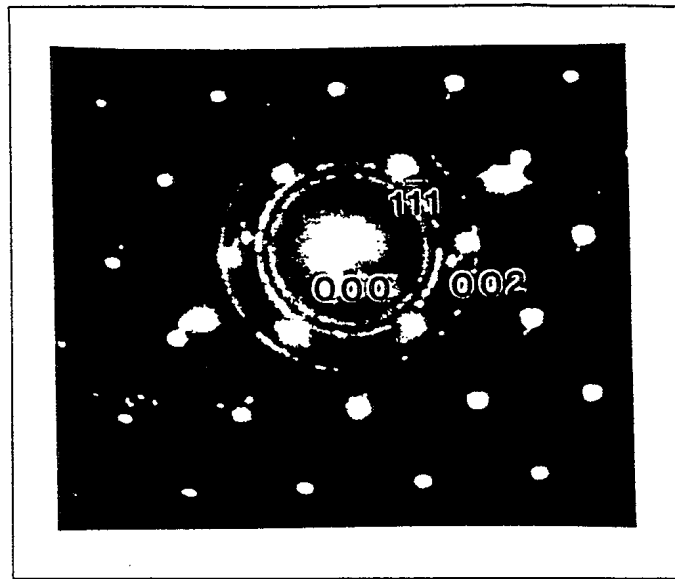
Figure 12: A "spotty" ring diffraction pattern produced by a collection of precipitates within a large SAD area-selecting aperture. The rings are superimposed on the [110] zone axis SAD pattern of the surrounding α matrix.
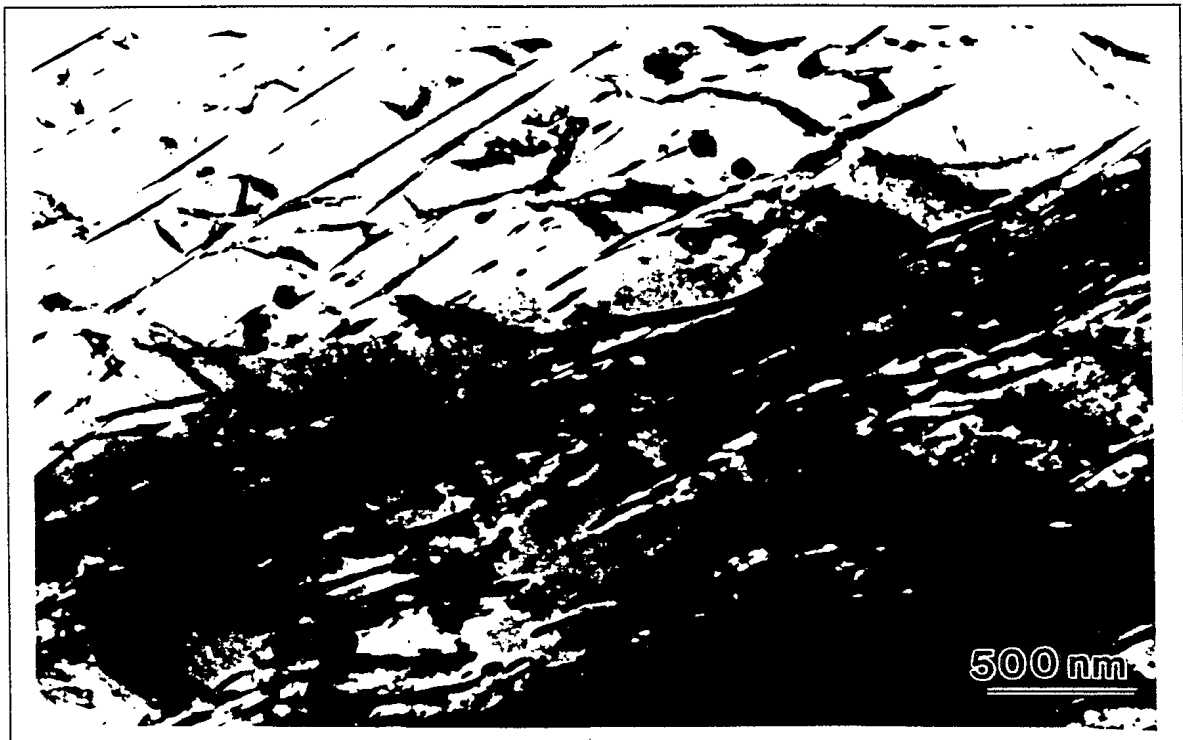

Figure 13: TEM image of a typical $(\alpha+\kappa_{III})$ eutectoid region in the reheat zone. The elongated particles are Ni-rich and have a B2 crystal structure.